ADVANCED MATERIALS

Supporting Information

for *Adv. Mater.,* DOI: 10.1002/adma.201402867

Biologically Inspired, Sophisticated Motions from Helically Assembled, Conducting Fibers

Peining Chen, Yifan Xu, Sisi He, Xuemei Sun, Wenhan Guo, Zhitao Zhang, Longbin Qiu, Jianfeng Li, Daoyong Chen, and Huisheng Peng**

WILEY-VCH

Supporting Information

Biologically inspired, sophisticated motions from helically assembled, conducting fibers

Peining Chen, Yifan Xu, Sisi He, Xuemei Sun, Wenhan Guo, Zhitao Zhang, Longbin Qiu, Jianfeng Li, Daoyong Chen, Huisheng Peng**

State Key Laboratory of Molecular Engineering of Polymers, Department of Macromolecular Science and Laboratory of Advanced Materials, Fudan University, Shanghai 200438, China; E-mail: lijf@fudan.edu.cn, penghs@fudan.edu.cn.

This PDF file includes:

Movies S1 to S9
Figures S1 to S21

Descriptions of supporting movies

Movie S1. Preparation of a helical primary fiber from a spinnable MWCNT array.

Movie S2. The flapping motion of an artificial wing prepared from a secondary fiber. The seconary fiber is twisted from 25 primary fibers with secondary helical angle of 31°. The pulse currents with the same magnitude of 50 mA but increasing frequencies of 0.25, 1, 5, and 10 Hz are passed through the secondary fiber.

Movie S3. The rotary motion of an electrically driven motor prepared from a self-twisted secondary fiber with primary, secondary, and tertiary helical angles of 32°, 31°, and 14°, respectively. A glass bar with weight of 1 g (5000 times of the tertiary fiber in weight) is attached at the folded point. The maximal rotary angle of the tertiary fiber reachs approximately 180° upon pass of a crrent of 125 mA.

Movie S4. The wagging motion of an artificial tail prepared from a self-twisted fiber. The tertiary fiber showed primary, secondary, and tertiary helical angles of 32°, 31°, and 14°, respectively. The two fiber ends are fixed on the horizontal edge, and a current with manitude of 125 mA and frequency of 1 Hz is passed through the fiber.

Movie S5. The wagging motion of an artificial tail that was traced by high-speed cameras upon the pass of a pulse current. The magnitude and frequency of the current are 140 mA and 1Hz, respectively. The motions at X-Y and X-Z planes are simultaneously demonstrated and re-constructed through a frame-by-frame analysis. The artificial tail had a similar structure with that used in Movie S4.

Movie S6. The wagging motion of an artificial tail that was traced by high-speed cameras upon the addition of a linear current. The scan rate of the linear current is 117 mA/s. The motions at X-Y and X-Z planes are simultaneously demonstrated and re-constructed through a frame-by-frame analysis. The artificial tail is the same as Movie S5.

Movie S7. The rotary actuation of the two ends of a secondary fiber upon pass of a pulse current with a magnitude of 100 mA and a period of 2 s. The secondary fiber is twisted from 50 primary fibers with diameter of ~115 μm and secondary heilcal angle of ~25°.

Movie S8. The dependence of the rotary actuation on the increasing current of 50, 100, and 150 mA. The secondary fiber is twisted from 50 primary fiber with length of 5 cm and secondary helical angle of 32°. A paper bar with width of 1 cm is symmetrically glued onto the MWCNT fiber at the top one-fifth position.

Movie S9. The electromechanical actuation in the water for a secondary fiber. The secondary fiber is twisted from 50 primary fibers with a diameter of ~115 μm and a secondary helical angle of 32 º. A cuurent with a magnitude of 100 mA and a period of 2 s is passed through the fiber.

Experimental Section

Preparation of the primary fiber. The primary fiber was prepared from spinnable MWCNT arrays that were synthesised by chemical vapour deposition. In a typical synthesis, Fe (1 nm)/Al_2O_3 (10 nm) deposited on a silicon substrate by electron-beam evaporation was used as the catalyst, ethylene with a flowing rate of 90 sccm was used as carbon source, and a mixture of Ar (400 sccm) and H_2 (30 sccm) was used as carrying gas. The synthetic reaction was performed at 740 ℃ for 15 min in a tube furnace, and a spinnable MWCNT array with a thickness of approximately 250 μm was obtained. The primary fibers could be dry-spun from the MWCNT array with increasing helical angles of 8°, 16°, 32°, 37°, and 43° by increasing the rotation speed to 500, 1000, 2000, 2500, and 3000 revolutions per minute (rpm), respectively (Figure S1 and Movie 1). The rotary speed of the collecting drum was the same (3 rad/min). The non-helical primary fibers were directly drawn from the array without rotation prior to passing through the alcohol. The diameters of the primary fibers were controlled by varying the width of the starting ribbon. The same width of approximately 1 cm was used to produce fibers with diameters of 15-17 μm after the ethanol treatment.

Preparation of the secondary fiber. Parallel primary fibers were stacked together with one end stabilised and the other in a rotating motor (Figure S2). Both left- and right-handed helical structures could be produced by anticlockwise and clockwise rotations, respectively. The secondary fibers with a left-handed helical structure were primarily used unless specified. A series of secondary fibers with increasing helical angles of 6°, 19°, 24°, 31°, 37°, and 43° were obtained by varying the rotary speed and time. The secondary fibers were treated with ethanol prior to use. The secondary fiber was generally over-twisted during preparation; thus, it further self-twisted after the two ends were assembled together.

Characterization. The sizes and structures were characterised by SEM (Hitachi FE-SEM S-4800, operated at 1 kV). The rotary actuation was monitored by optical microscopy (Olympus BX51). The movies were recorded using a digital camera (Canon EOS 500D). For the mechanical measurement, the fiber was fixed to a paper hole with a gauge length of 5 mm using silver paste and tested on the HY0350 Table-top Universal Testing Instrument with a tensile rate of 1 mm/min.

To measure the contractive actuation, the fiber was fixed to a paper hole with a gauge length of 5 mm using silver paste, and two copper wires were connected to the fiber (Figure S11). The fiber was measured with a table-top testing instrument (HY0350 Table-top Universal Testing Instrument), and the electrically actuated contractive force was traced in situ. The pulse current was provided by a Keithley Model 2400 Source Meter.

Because the rotary angles varied at different locations along the fiber, a paper bar stabilised at the top one-fifth of a 5-cm-long fiber had been used to measure the rotary actuation. As shown in Figure S13, the secondary fiber was stretched by two clamps, and the paper bar with a length of 1 cm was stabilised in the middle. The rotary motion of the paper bar was recorded using a digital camera (Canon EOS 500D). Through a frame-by-frame analysis, the rotary angles (γ) with increasing pulse currents were calculated by the equation $\gamma = 90° - \arcsin(d/l)$, where l=5 mm (i.e., half the length of the paper bar) and d corresponds to the projected length.

Flapping motion of an artificial wing. The secondary fiber was prepared by winding 25 helical primary fibers (with a primary helical angle of 32 °) with a secondary helical angle of approximately 31 °. The two ends of the bent secondary fiber were fixed on a horizontal edge. The fiber was connected to the external circuit by copper wires (Figure 2a), and the pulse current was provided by a Keithley Model 2400 Source Meter. For the bent fiber, the rotary directions of the two ends were both anticlockwise. As a result, the blue paper attached to the bent fiber flapped up when the current was passed through the fiber and flapped down after the current was disconnected. The flapping angle (α) was determined by the equation $\alpha = \arcsin(d/l)$, where l and d correspond to the maximal length of the wing (5.5 mm) and its vertical projection length, respectively.

Rotary motion of the artificial motor. The electrically driven motor was prepared from a secondary fiber. As shown in Figure S4, a glass bar with weight of 1 g was attached at the folded point of the fiber, and a current of 125 mA was passed through the fiber.

Wagging motion of the artificial tail. The artificial tail was easily prepared from a self-twisted fiber. The two ends of the fiber (with primary, secondary, and tertiary helical angles of 32 °, 31 ° and 14 °, respectively) were fixed on a horizontal edge. The fiber was connected to the external circuit by copper wires. The motion of the tail end was traced by two high-speed cameras in the vertical and horizontal directions. The re-construction of the motion was produced by frame-by-frame analysis and Matlab software. The pulse and linear electric currents were provided by a Keithley Model 2400 Source Meter.

The trajectory of the tail end was similar to an arc and can be described by the motion of the angle (Figures S8 and S9) using an exponential decay equation: $\theta(t)=\theta_{eq}+\Delta\theta e^{-t/\tau}$. The motion equation can be obtained as follows:

$$\frac{d\theta(t)}{dt}=-k(I_0)[\theta(t)-\theta_{eq}(I_0)] \qquad \text{(S1)}$$

where $k(I_0)=\tau^{-1}$ depends on the current and θ_{eq} is the equilibrium angle of the end point. By fitting the experimental data, k and $|\Delta\theta|$ are calculated as 30 s^{-1} and 1.3, respectively, at an I_0 of 140 mA. When the power is off, the motion of the end point is governed by the same equation but with a much slower angular speed ($k \approx 8$ s^{-1} and $|\Delta\theta| \approx 1.0$). According to the scaling analysis, a quadratic power law is assumed for the linear current and still holds true for $k(I_0)\propto I_0^2 \propto t^2$; thus, the motion equation becomes the following:

$$\frac{d\theta(t)}{dt}=-\alpha t^2[\theta(t)-\theta_{eq}] \qquad \text{(S2)}$$

Actuating properties

Primary fiber. The electromechanical actuation could be completed in millisecond and further traced in situ (Fig. S11). The primary fiber did not generate an obvious stress below ~2 mA while produced a significant increase beyond this point (Fig. S12a). An equation of F $\propto$ I^2 was concluded with F and I as produced stress and current, respectively. The relationship between the produced stress and helical angle was also studied, i.e., as shown in Figure S12b, upon addition of the same current of 5 mA, the contractive stress was first increased and then decreased with the increasing helical angle, and a peak value was appeared at a primary helical angle of 32^o. Therefore, the primary fibers with helical angles of 32^o were further twisted to form the desired secondary fibers. The rotary angle was measured from a 5-cm-long primary fiber with a helical angle of 32^o (Fig. S13). As the rotary angle varied along the fiber, the position at the top one-fifth had been used for measurements. The rotary angles were continuously increased to 4.5^o, 8^o, 12.5^o, 19.2^o, 25.6^o and 34^o when the currents were enhanced to 4, 5, 6, 7, 8 and 9 mA, respectively (Fig. S14).

Secondary fiber. The applied stress had greatly affected the generated contractive stress. For instance, Fig. S20 shows the dependence of the contractive stress on the applied stress for a secondary fiber with helical angle of appropriately 31^o upon the pass of 125 mA. The contractive stress was increased sharply when the applied stress is lower than 10 MPa and then gradually increased with the further increase of applied stresses. This phenomenon can be explained by the fact that primary fibers are relatively stretched loosely at low applied stresses, and the actuations of some primary fibers are transported to generate contractive stresses. However, the contributing primary fibers were greatly increased below the critical point, so a sharp increase in the contractive stress was observed. According to the Ampere's Law, the relationship between Ampere's force (F) and distance (d) between current vectors can be expressed by $F \propto d^{-1}$ (Equation (3) at the main text). The contractive stress was further increased with the further increase of applied stress beyond the critical point as the distance among the assembled primary fibers was reduced. The above conclusions are also verified by the theoretical simulation and discussed later. For convenience, the same load of 20 MPa was applied to the primary and secondary fibers in this work unless specified.

Simulation

A non-helical primary fiber has been firstly studied for the simplicity. A scaling analysis based on Ampere's Law and the principle of virtual work is made to understand the electromechanical contraction and torsion. Helically paralleled MWCNTs were found to shrink upon pass of electric currents due to Ampere's Law. On the other hand, for the fibers composed of non-helical MWCNTs, there should be no electromagnetic forces along the axial direction because the Lorentz force is always perpendicular with the current. However, according to the Law of the Lever or the principle of virtual work (Figs. 4e-g), the perpendicular electromagnetic force exerted on aligned MWCNTs can be transferred to a contractive force. As can be seen from Figs. 4e-g, although the electromagnetic force F_{B} exerted on the labelled MWCNT (blue dot in Fig. 4e) is small and perpendicular with axial direction, it will generates a much bigger force F_{C} along the axial direction if there are some fulcrums (denoted by two triangles in Figs. 4f-g) stuck between the MWCNT and nearest MWCNT bundle. According to the principle of virtual work or the law of the lever, F_{C} can be magnified to the order of l/d compared with F_{B} and this force together the magnified forces exerted on other MWCNTs will certainly cause the fiber to shrink. Detailed deductions of F_{B} and F_{C} will be presented in the following text.

Consider an MWCNT, labelled as a blue dot, and a neighboring bundle of MWCNTs with a cross-sectional radius of r (Fig. 4e). According to Ampere's Law, the electromagnetic force between a small section of the labelled MWCNT with the length Δx and the MWCNT bundle can be calculated as

$$F_B(r, \Delta x) = \frac{\mu_0 I_r I_1}{2\pi r} \Delta x \quad \text{(S3)}$$

where μ_0 is the permittivity of air. The electric currents inside the labelled MWCNT and inside the bundle are connected to the current I_0 passing through the whole fiber by the relations of $I_1 = \frac{I_0 \Delta A}{A}$ and $I_r = \frac{I_0 r^2}{R^2}$, respectively, where ΔA and $A = \pi R^2$ are the effective cross-sectional areas of the labelled MWCNT and the whole fiber.

Critical actuating current. When the force exceeds some critical value, the labelled MWCNT will bend to the circled MWCNT bundle (Fig. 4g). It is expected that, at the critical point, the energy of the magnetism should be comparable to the bending energy of the MWCNT, i.e. $E_{mag} \approx E_b$. According to $E_{mag} \sim I_0^2$ and $E_b \sim \kappa$, where κ is the bending rigidity of the MWCNT, the critical actuating current depends on the bending rigidity with the scaling law of

$$I_0 \propto \kappa^{1/2} \qquad \text{(S4)}$$

Amplification of Electromagnetic Force. Just as discussed previously, if there are fulcrums (entangling points) between the labelled MWCNT and the bundle, F_B can be transferred to the force F_C along the axial direction and will be magnified to the order of l/d. Luckily, MWCNTs inside a non-helical bundle are indeed not perfectly aligned along the axial direction. In other words, there exist some entanglements, acting as fulcrums of the lever (denoted by two small blue triangles in Figs. 4f-g), between the labelled MWCNT and the circled MWCNT bundle. If the average distance between these two points is l, the work done by the magnetism that pushes the MWCNT to deform from Fig. 4f to Fig.4g can be calculated as below,

$$W = 2\int_0^{l/2} \frac{\mu_0 I_1 I_r dx}{2\pi r}\left(\frac{x}{l/2}\right) d = \frac{\mu_0 I_1 I_r ld}{4\pi r} \qquad \text{(S5)}$$

Based on the energy conservation, this work is equal to the work that causes the labelled MWCNT to shrink with the length $2d^2/l$, i.e. $W = 2F_C(r)d^2/l$. Then the force exerted on the labelled fiber can be obtained,

$$F_C(r) = \frac{Wl}{2d^2} = \frac{\mu_0 I_0^2 \Delta A r l^2}{8\pi R^2 A d} \qquad \text{(S6)}$$

Obviously, $F_C(r) = F_B l/2d$ if $F_B \equiv \mu_0 I_1 I_r l/2\pi r$, which indicates the magnetism force has been amplified by $l/2d$ times.

Summing over the contractive forces of every MWCNTs inside the fiber, the shrinkage force exerted on the whole non-helical fiber is calculated as follow,

$$F = \int \frac{\mu_0 I_0^2 \Delta A' r l^2}{8\pi R^2 A d} = \int \frac{\mu_0 I_0^2 r^2 l^2 dr}{4R^2 A d}$$
$$= \frac{\mu_0 I_0^2 l^2}{12\pi R d} \quad \text{(S7)}$$

Note that $\Delta A'$ has been defined as $2\pi r dr$ instead.

Finally, the stress can be calculated as

$$\sigma = \frac{F}{A} = \frac{\mu_0 I_0^2 l^2}{12\pi^2 R^3 d} \quad \text{(S8)}$$

where $\mu_0 = 4\pi \times 10^{-7}\,\mathrm{N \cdot A^{-2}}$. According to the experiment, the radius of the primary fiber (R) is 8 μm and the distance among MWCNTs (d) is approximately 100 nm. Here the average l is considered as a persistence length of the primary fiber, which may be related to the mechanical property of the fiber. In the current work, the contractive stress of the non-helical primary fiber is ~3.3 MPa when a current of 5 mA is applied, so l is calculated to be 2.52 cm according to Equation (S8). If the scaling law of Equation (S8) is true, it is critically important to improve the contractive stress by increasing the value of l.

Helical primary fiber. Consider a helical primary fiber consisting of N MWCNTs. We can divide these N MWCNTs into n MWCNT bundles each with N/n MWCNTs. Although each MWCNT bundle is helical, the results of non-helical fiber (bundle) can be also applied if we focus on a small section of the helical bundle which can be approximated as a non-helical bundle. To this end, one can first employ the non-helical model to obtain the contractive force (or stress) and the contour-length contraction ΔL for each helical MWCNT bundle (Fig. S21 a-b); then the true contraction can be calculated as $\Delta L \cos\theta$ if the helical angle is θ (Fig. S21 c-d); finally the electromagnetic interactions between helical bundles will cause the helical bundle to shrink its helical radius, which will, instead, elongate the helical bundle a little bit. The net contractive force (stress) exerted on the helical primary fiber can be again calculated according to the principle of virtual work, i.e.

$$F_{net} \Delta Z = F_{non} \Delta L \quad \text{(S9)}$$

where ΔZ is the net shrinkage of the helical primary fiber in length, ΔL is the net contour-length shrinkage of the helical bundle. F_{non} can be obtained using the non-helical model (Equation (S7))

$$F_{non} = c_1 I_0^2 \quad \text{(S10)}$$

Note that the constant c_1 can be easily recovered using Equation (S7).

Now let's calculate net shrinkage ΔZ. Consider a helical MWCNT bundle labelled with *k*. The helical radius is expressed as R_{k0} prior to pass of the current (Fig. S21). After pass of the electric current, the helix *k* will be shortened by ΔL_k of its contour length; meanwhile, it will be dragged to the center of the primary fiber to certain degree due to the Lorentz force generated by the current. Therefore, the energetic gain and loss (including bending energy and electromagnetic energy) during this process can be calculated as

$$\Delta E = \frac{\kappa}{2}\left(\frac{\sin^2\theta}{R_k} - \frac{\sin^2\theta}{R_{k0}}\right)^2 L_k + \frac{\mu_0 I_k I_b L_k \cos\theta}{2\pi}\ln\frac{R_k}{R_{k0}} \qquad \text{(S11)}$$

Where κ, L_k and R_k correspond to the bending rigidity, length of the labelled MWCNT, and the helical radius when the current is applied, respectively (Fig. S21). I_k and I_b correspond to the current in the labelled MWCNT and the current inside the area with the radius of R_{k0}, respectively.

R_k can be further optimized by minimizing ΔE. As a result, the shrinkage of the labelled MWCNT in the radial direction can be calculated as

$$\Delta R = R_{k0} - R_k = \frac{\alpha I_0^2 R_{k0}\cos\theta}{2\alpha I_0^2\cos\theta + \kappa\sin^4\theta} \qquad \text{(S12)}$$

where $\alpha \equiv \mu_0 I_k I_0 R_{k0}^2 / 2\pi$. Note that $\Delta R/R_k \to 0$. The rotatory angle of the fiber with a length of *L* can be then estimated by

$$\Delta\phi(I_0) \sim \frac{\Delta R L\sin\theta}{R_{k0}^2} = \frac{L}{R_{k0}}\frac{\alpha I_0^2\cos\theta\sin\theta}{2\alpha I_0^2\cos\theta + \kappa\sin^4\theta} \qquad \text{(S13)}$$

For Fig. S17b, $L/R_{k0} = 10$, $\alpha = 100 N\cdot A^{-2}$, $\kappa = 40N$ and $\theta = 30°$.

At the same time, the net decrease of the primary fiber in length can be also calculated as

$$\Delta Z \approx \left(\Delta L_k - \frac{\Delta R L\sin^2\theta}{R_{k0}}\right)\cos\theta \qquad \text{(S14)}$$

The first part on the right hand side corresponds to the projected shrinkage of the labelled MWCNT along the axial direction while the second part corresponds to the stretch produced by the tightening effect of the helical MWCNT due to the Lorentz force.

Plugging Equation (S14) back into (S9), the net contractive force can be derived

$$F_z = F_{non}\Delta L_k / \Delta Z = F_{non}\frac{\Delta L_k}{(\Delta L_k - \frac{\Delta RL\sin^2\theta}{R})\cos\theta}. \qquad \text{(S15)}$$

Accordingly, the stress is magnified,

$$\begin{aligned}\sigma(\theta) &= \sigma_{non}\frac{\Delta L_k}{(\Delta L_k - \frac{\Delta RL\sin^2\theta}{R})\cos\theta} \\ &\equiv \sigma_{non}\frac{\cos\theta + a\sin^4\theta}{(\cos\theta + a\sin^4\theta - b\cos\theta\sin^2\theta)\cos\theta}\end{aligned} \qquad \text{(S16)}$$

Note that ΔL_k has been absorbed into the coefficients of *a* and *b*, and Equation (S10) has been employed in the above deduction.

Obviously, when the helical angle (θ) was constant, the rotary actuations quadratically depended on the electric current based on Equation (S13) (Fig. S17b), which agreed with the experimental observation (Fig. S14); when the electric current was constant for the primary fiber, according to Equation (S16), the relationship between $\sigma(\theta)$ and θ is shown in Fig. S17a at a = 3.5 and b = 3.5, which agrees well with the experimental data (Fig. S12b).

Secondary fiber. The contractive and rotary actuation of the secondary fiber can be explained by a similar mechanism. The contractive stress and rotatory angle are further amplified by the helical organization of primary fibers. For instance, the stress of the secondary fiber can be estimated as:

$$\sigma(\theta_s, \theta_p) = \sigma_{non} g(\theta_p) g(\theta_s) \qquad \text{(S17)}$$

where θ_p and θ_s are the primary helical angle and secondary helical angle, respectively, and

$$g(\theta) = \frac{\cos\theta + a\sin^4\theta}{(\cos\theta + a\sin^4\theta - b\cos\theta\sin^2\theta)\cos\theta}. \qquad \text{(S18)}$$

Obviously, for the secondary fiber, the simulated results in the contractive and rotary actuations were similar to those shown in Figure S17 and consistent with the experimental observations (Figures 4a and b)

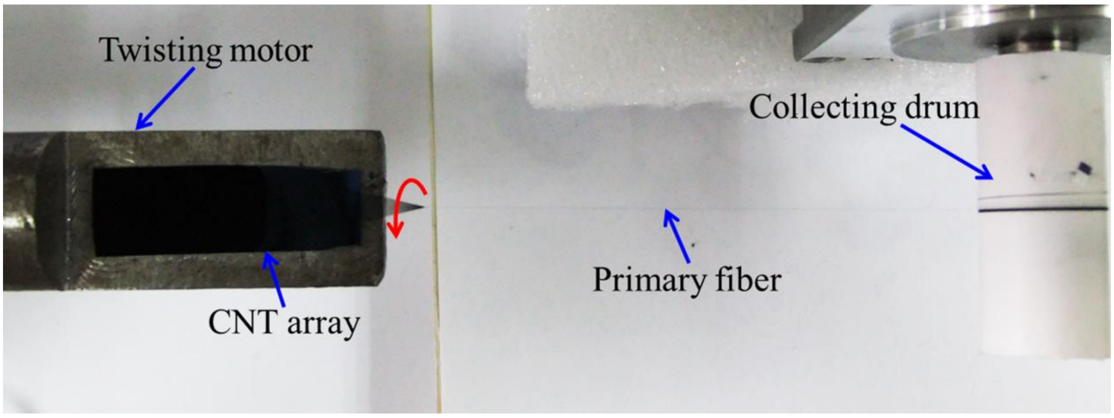

Figure S1. Photograph of the experimental setup to prepare a primary MWCNT fiber.

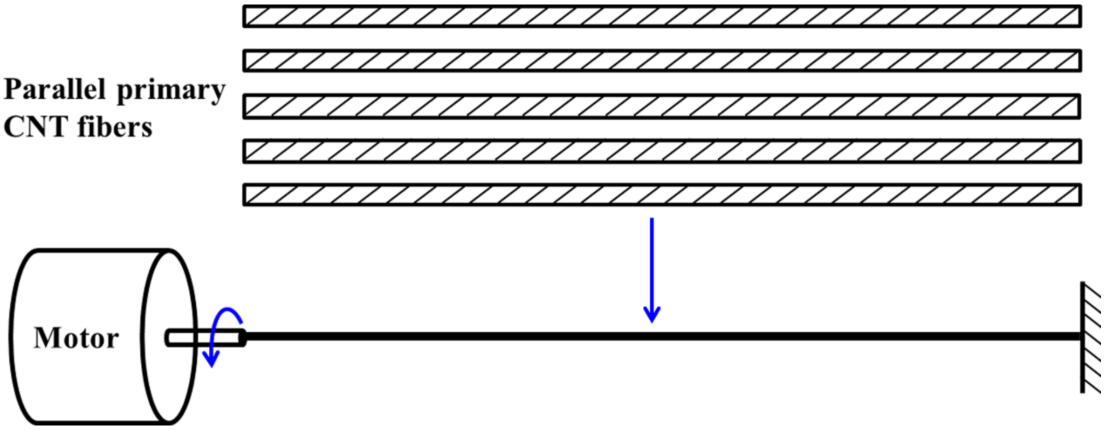

Figure S2. Schematic illustration of the experimental setup to prepare a secondary fiber.

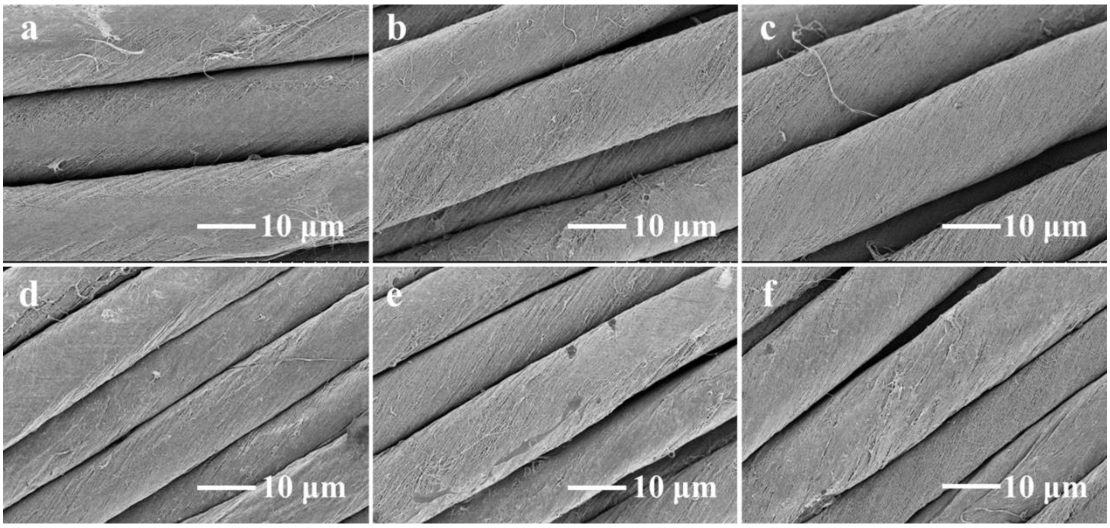

Figure S3. SEM images of secondary fibers with increasing secondary helical angles of appropriately 5 º(**a**), 19 º(**b**), 24 º(**c**), 31 º(**d**), 37 º(**e**), and 43 º(**f**).

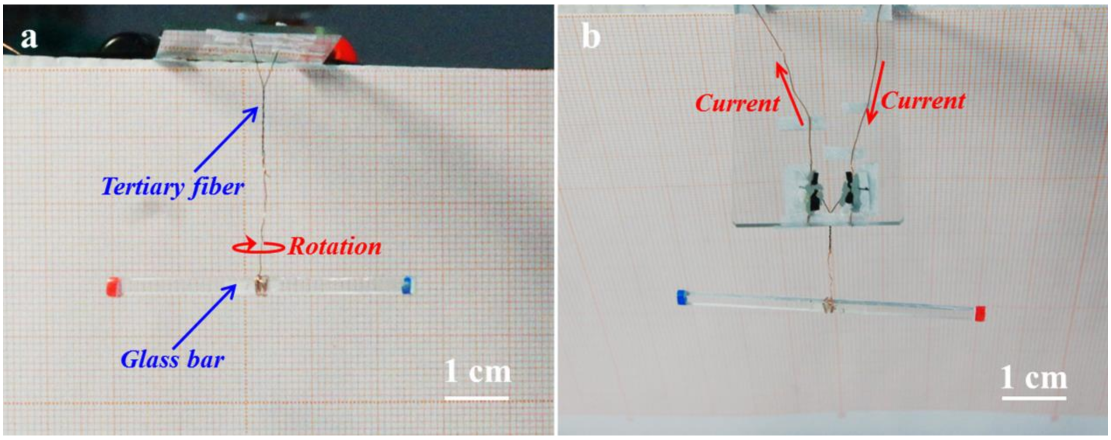

Figure S4. Photographs for the experimental setup of the rotary motor prepared from a self-twsited secondary fiber by side (**a**) and oblique (**b**) views.

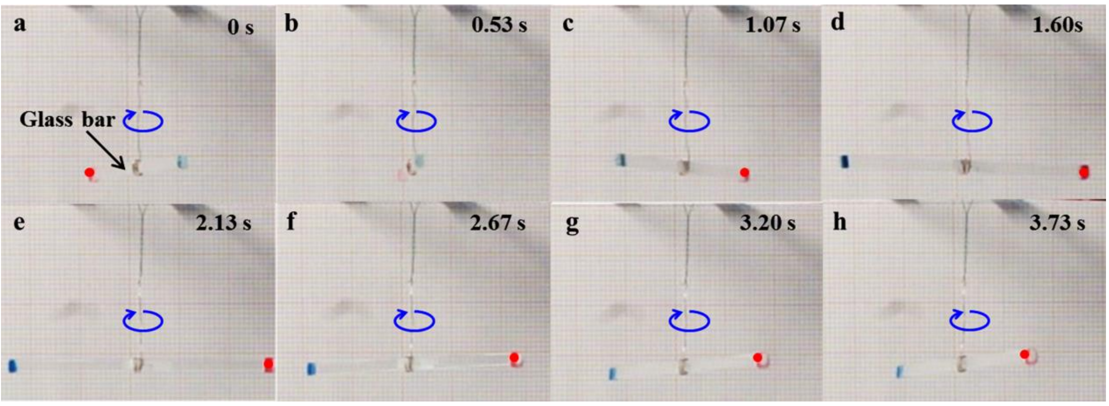

Figure S5. Photographs of the motion trail of a rotary motor based on the self-twisted secondary fiber upon pass of a current of 125 mA in a period of 10 s. The current was turned on at 0 s.

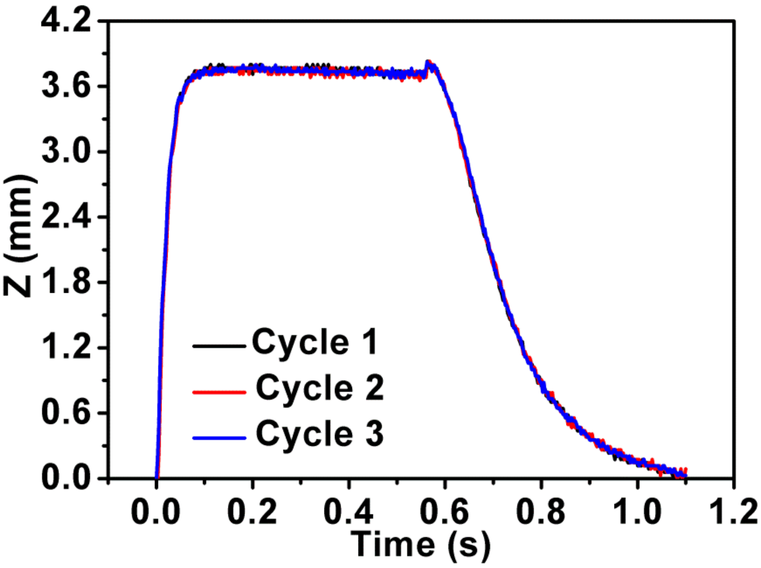

Figure S6. Dependence of the displacement along the Z axis on time for three cycles.

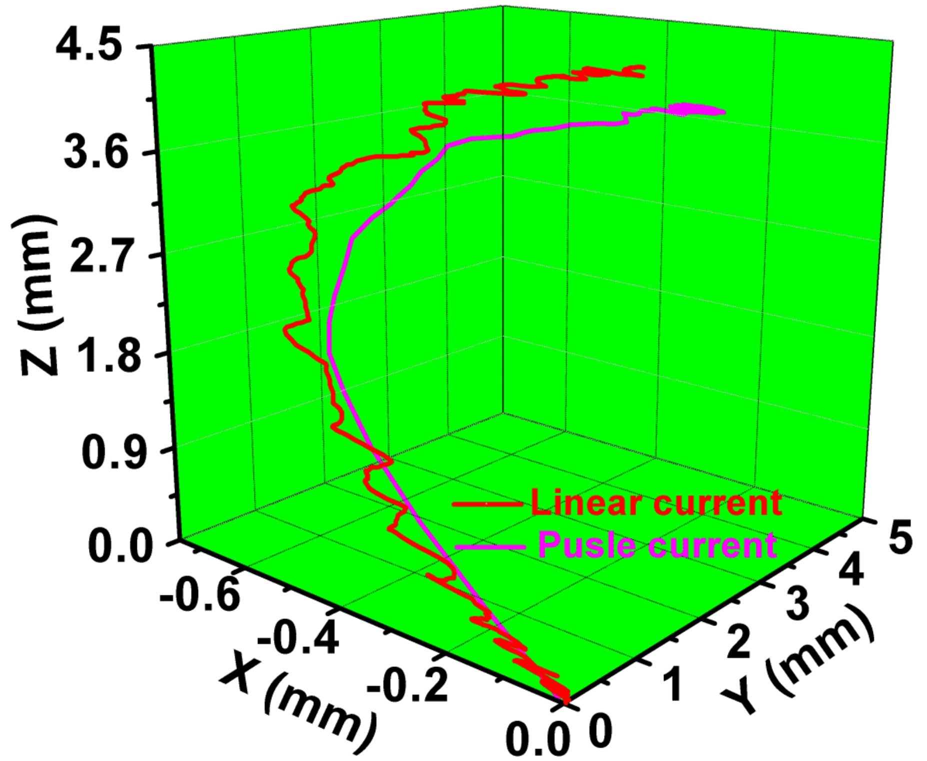

Figure S7. Three-dimensional trajectories of the motion at the tail end when pulse and linear currents are applied.

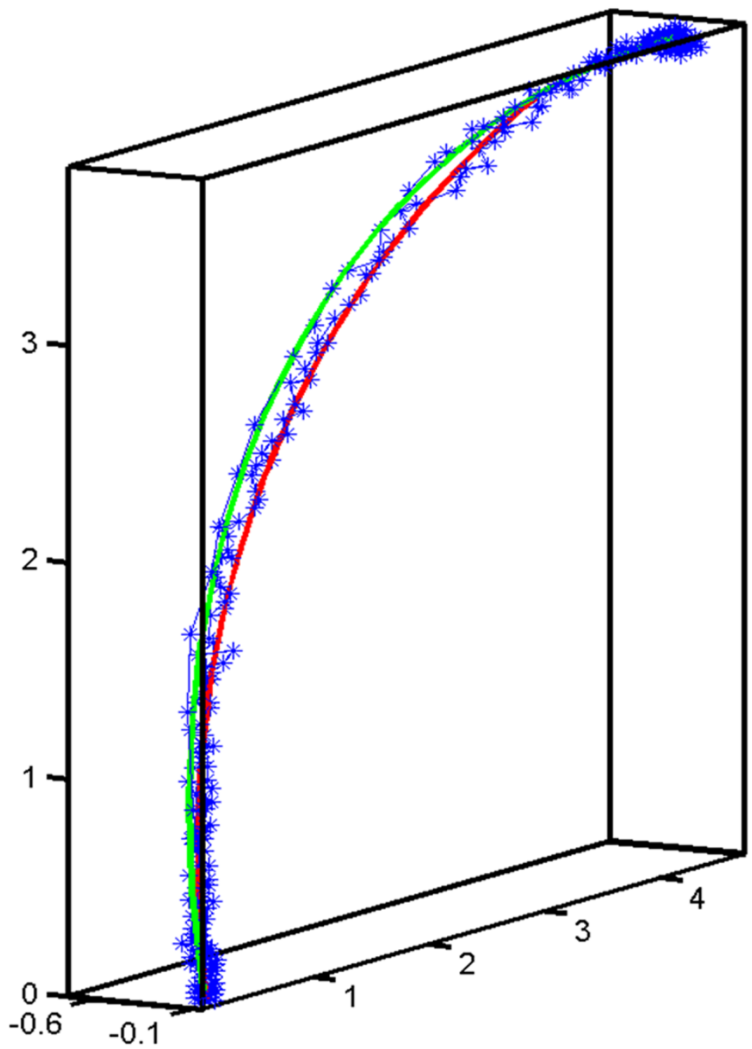

Figure S8. Approximately arc motions of the tail end upon pass of a pulse current. The green and red curves are plotted from Equation (1) at the main text when the power is turned on and off, respectively. The blue dots correspond to the experimental data.

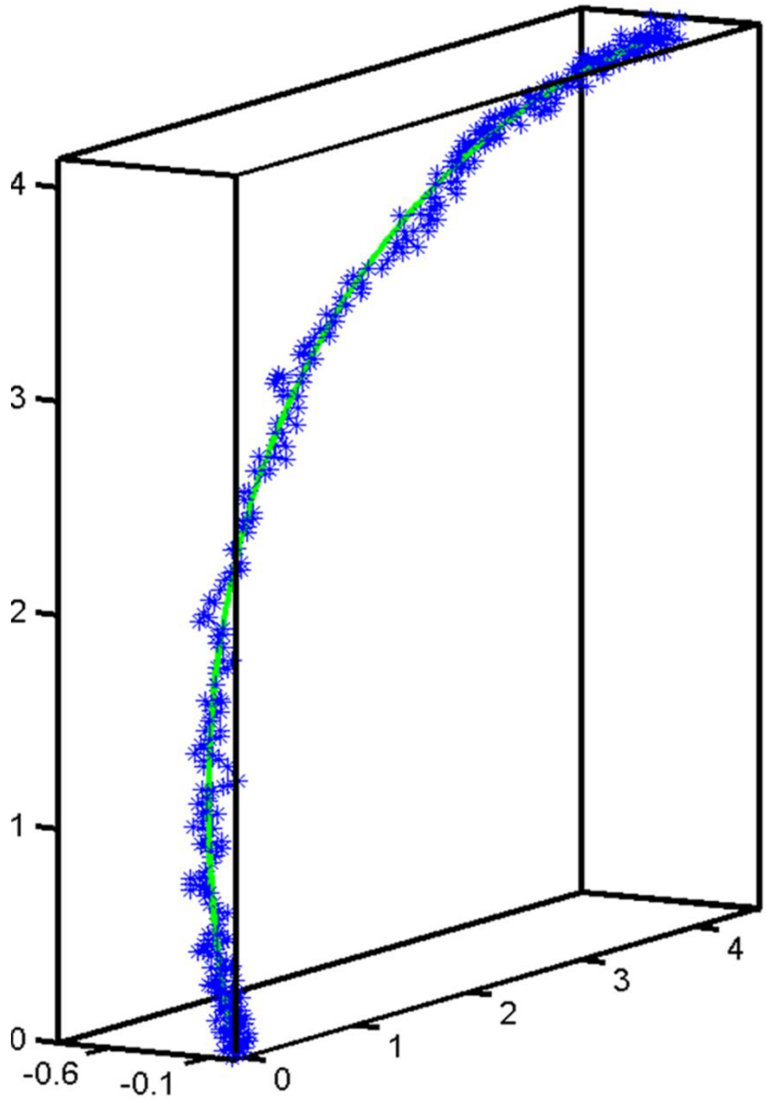

Figure S9. Approximately arc motions of the tail end upon pass of a linear current. The green curve is plotted from Equation (2) at the main text when the power is turned on. The blue dots correspond to the experimental data.

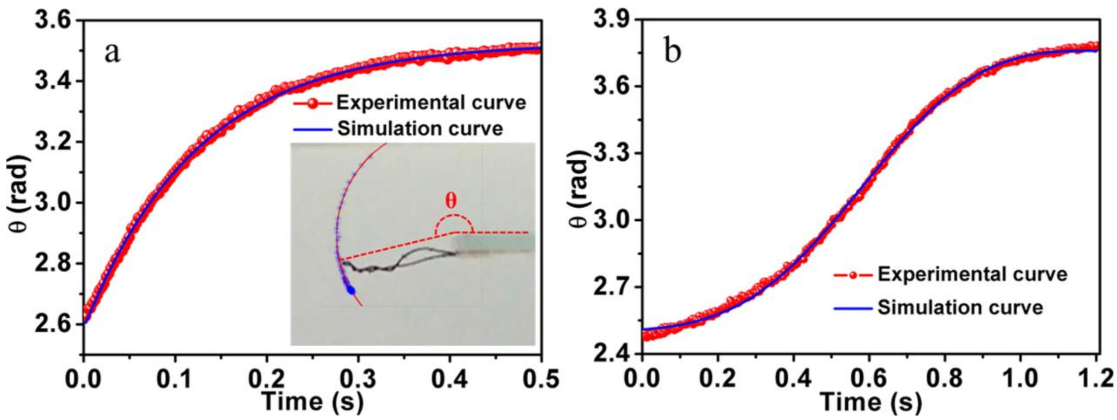

Figure S10. a) Dependence of the swinging angle on time (red line) when a pulse current is applied. The simulation curve (blue line) is obtained from Equation (1) at the main text. **b**) Dependence of the swinging angle on time (red line) when a linear current is applied, and the simulation curve (blue line) is obtained from Equation (2) in the main text.

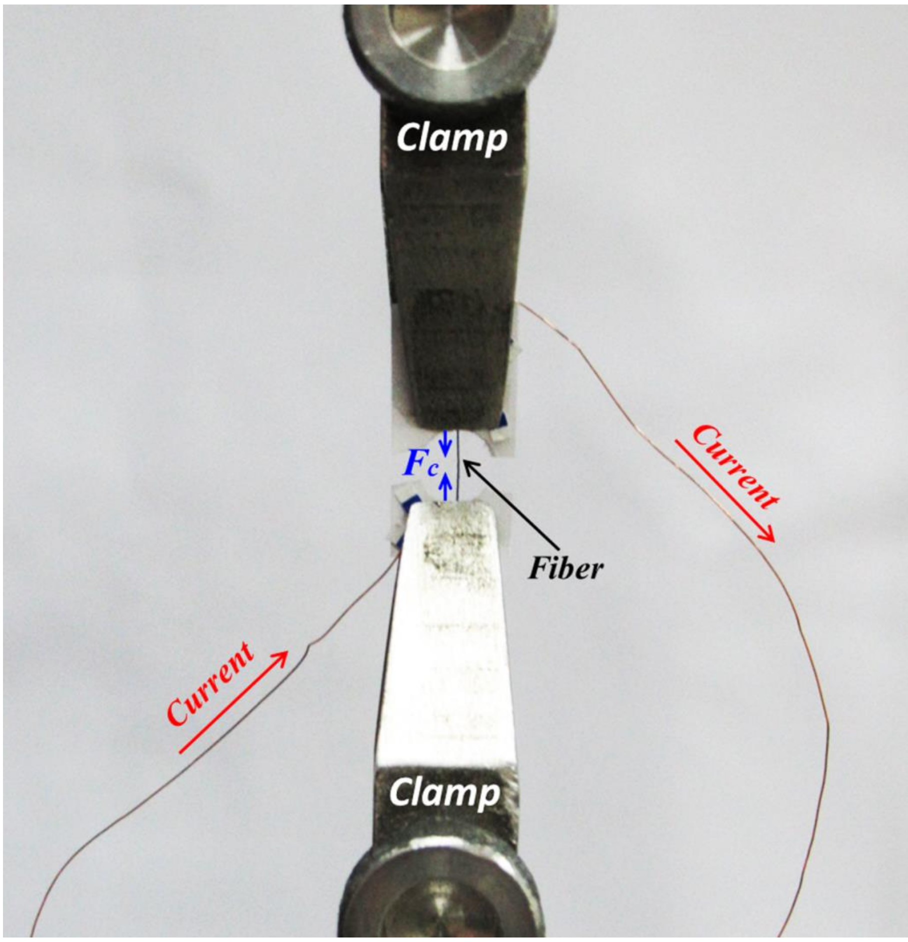

Figure S11. Photograph of the experimental setup for the measurement of the contractive force produced by the primary fiber.

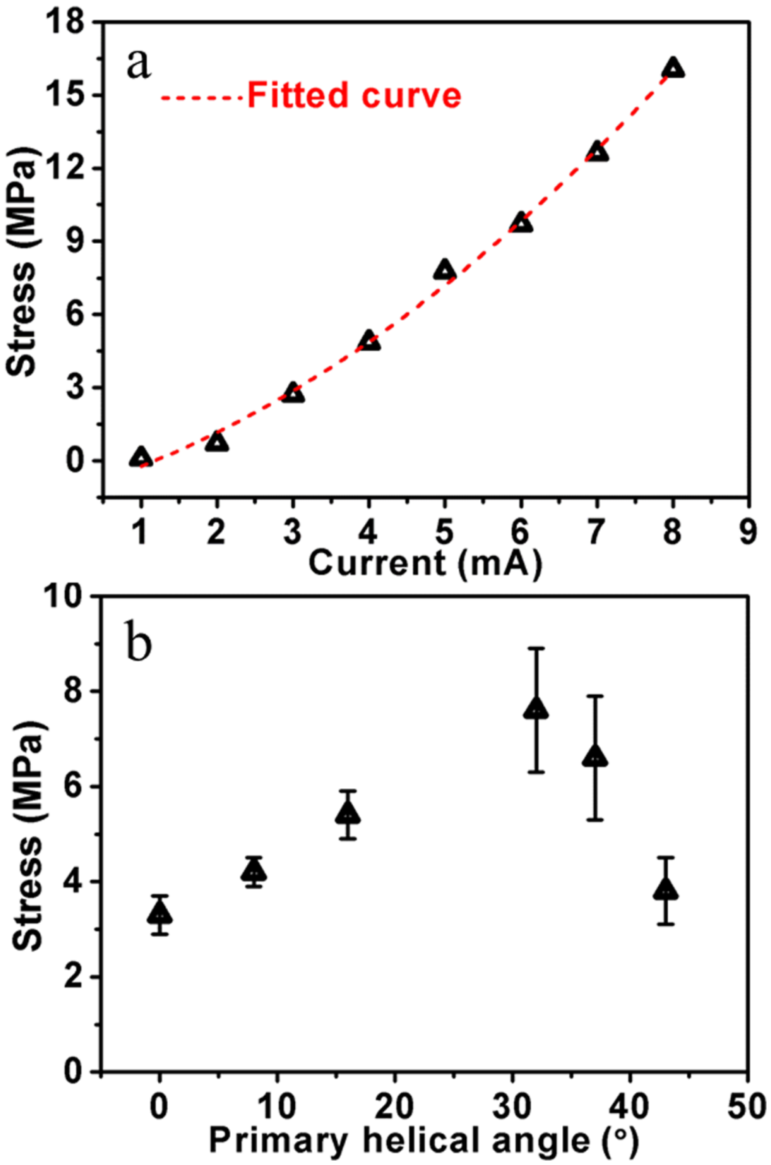

Figure S12. a) Dependence of the contractive stress on the current magnitude. **b**) Dependence of the contractive stress on the helical angle under the same passed current of 5 mA. The fiber shared a length of 5 mm at (**a**) and (**b**). The fiber at (**a**) had a primary helical angle of 32 º.

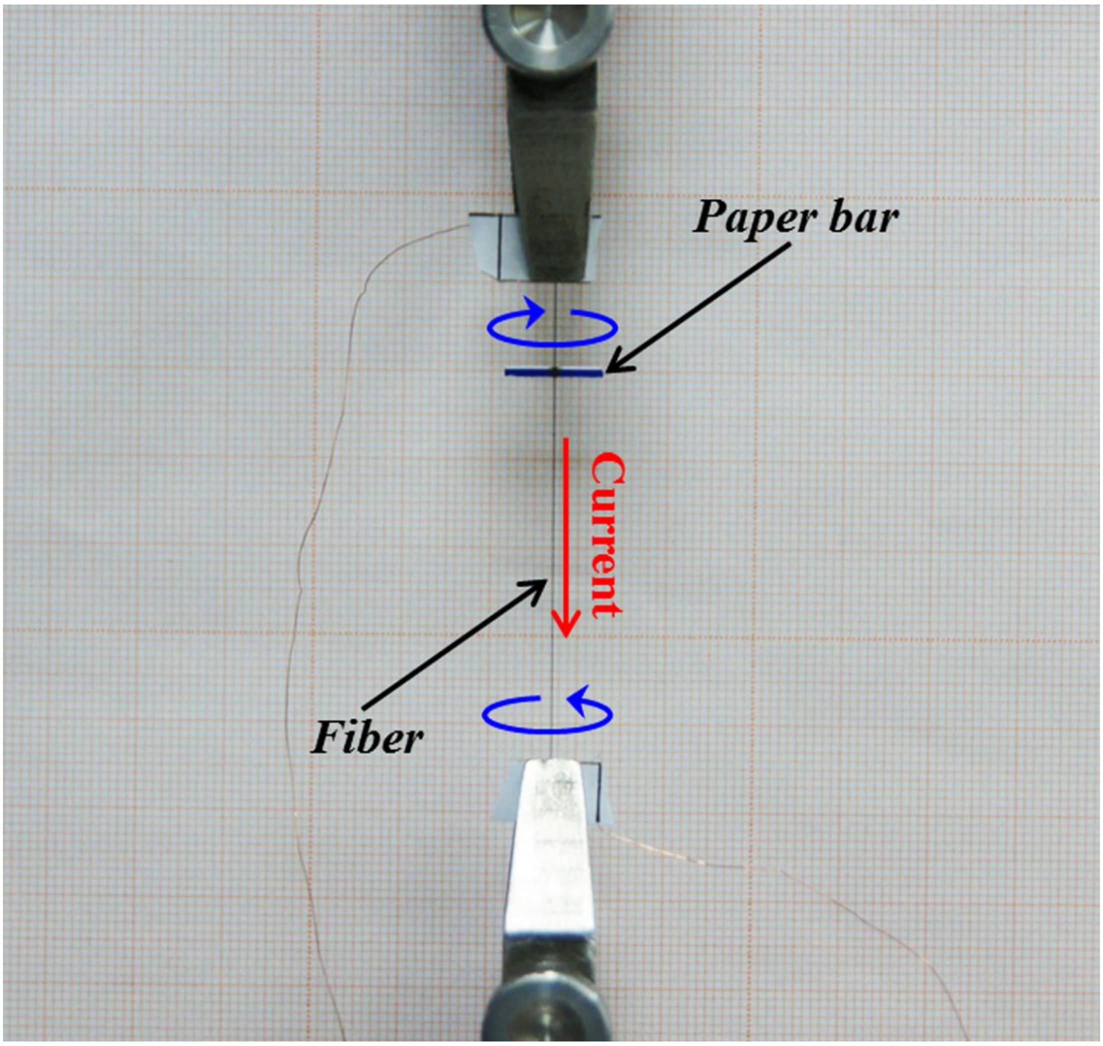

Figure S13. Photograph of the experimental setup for the measurement of rotary angles. A paper bar is fixed on the primary fiber.

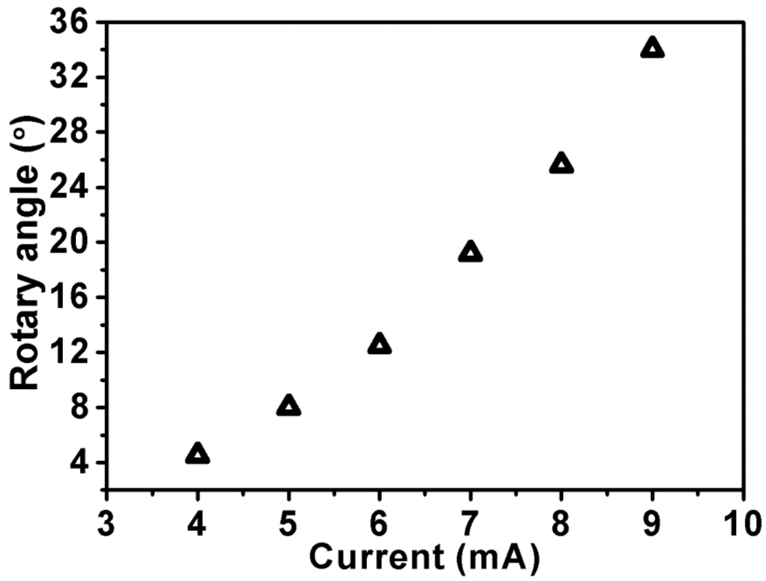

Figure S14. Dependence of the rotary angle on the current at the top one-fifth part. The primary fiber had a helical angle of 32 °and length of 5 cm.

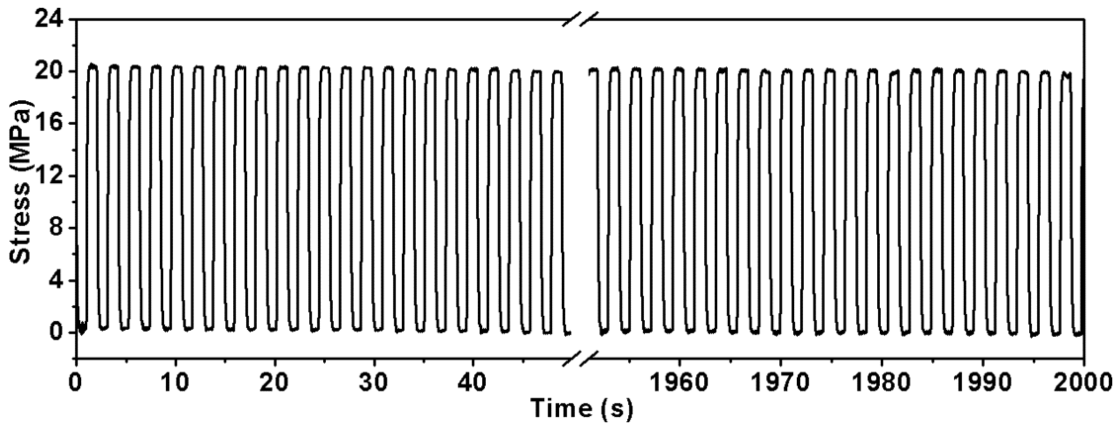

Figure S15. Contractive stresses for 1000 cycles at a current of 125 mA and frequency of 0.5 Hz.

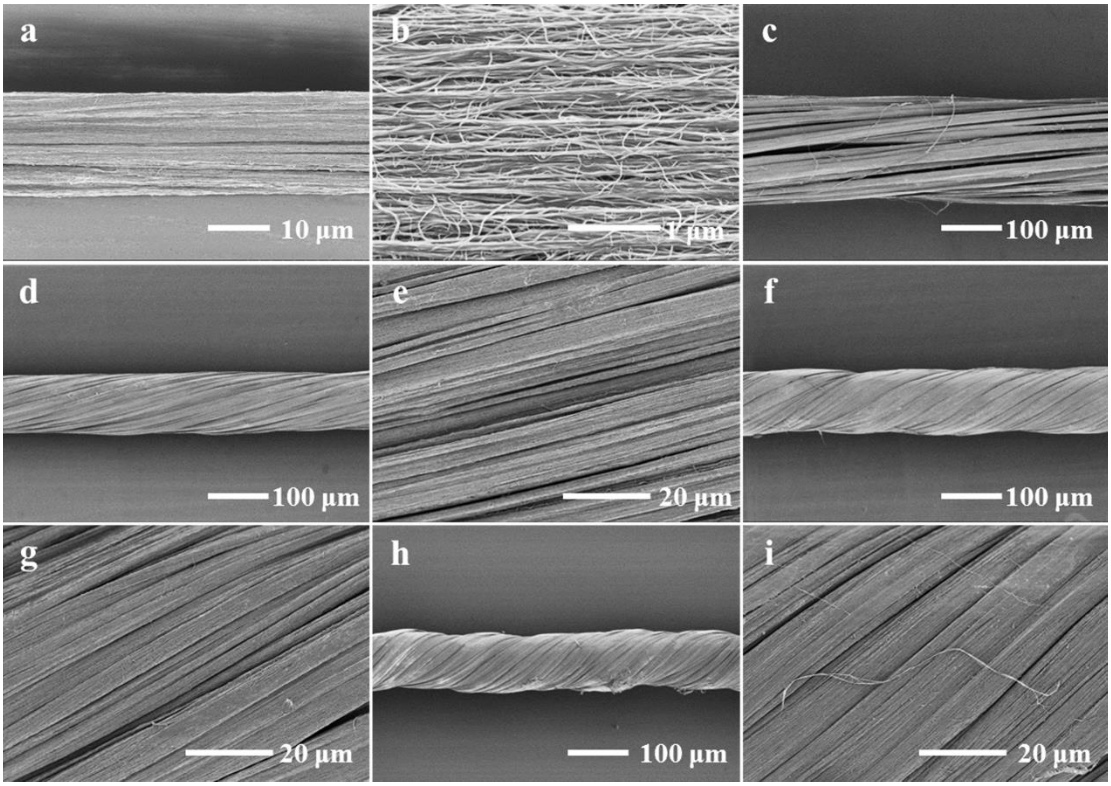

Figure S16. SEM images of secondary fibers that were prepared by twisting 50 non-helical primary fibers. **a**, **b**) A non-helical primary fiber at low and high magnifications, respectively. **c**), **d**), **f**), and **h**) Secondary fibers with increasing secondary helical angles of appropriately 5 °, 15 °, 28 °and 35 °, respectively. **e**), **g**) and **i**) Higher magnifications of (**d**), (**f**), and (**h**), respectively.

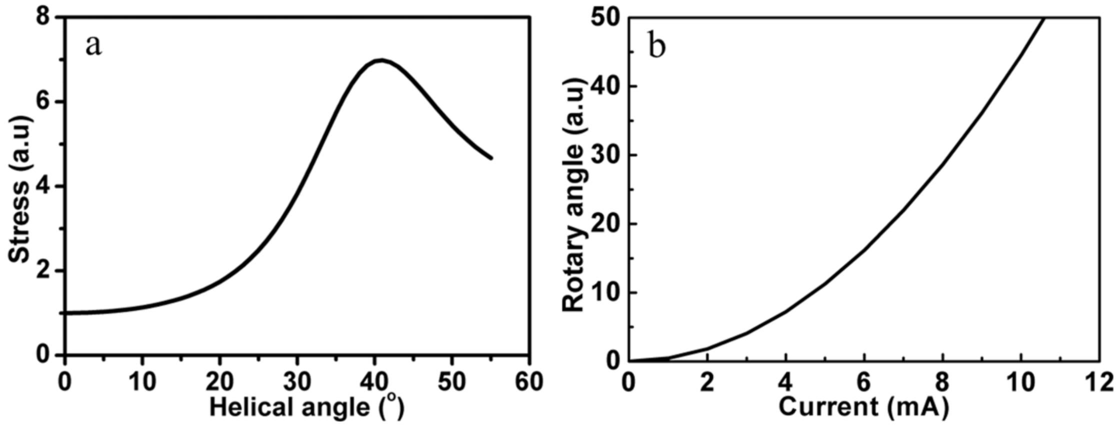

Figure S17. a) Dependence of the contractive stress on the helical angle based on the scaling theory (Equation (3) in the main text). **b**) Dependence of the rotatory angle on the magnitude of current according to Equation (4) in the main text.

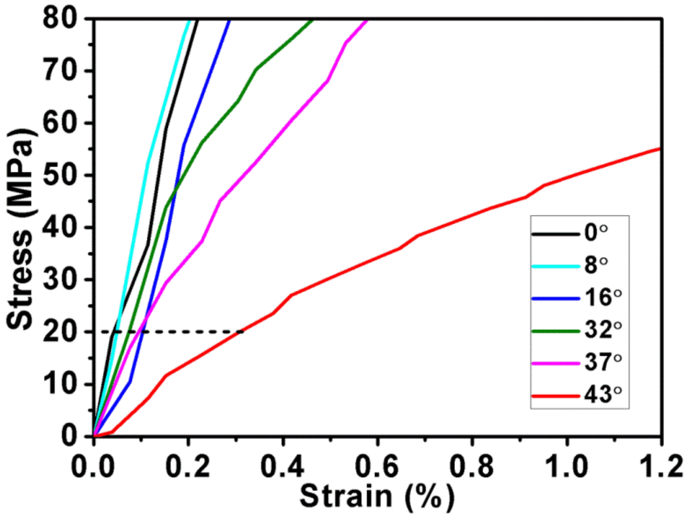

Figure S18. Stress-strain curves of the primary fibers with increasing primary helical angles at the starting stage.

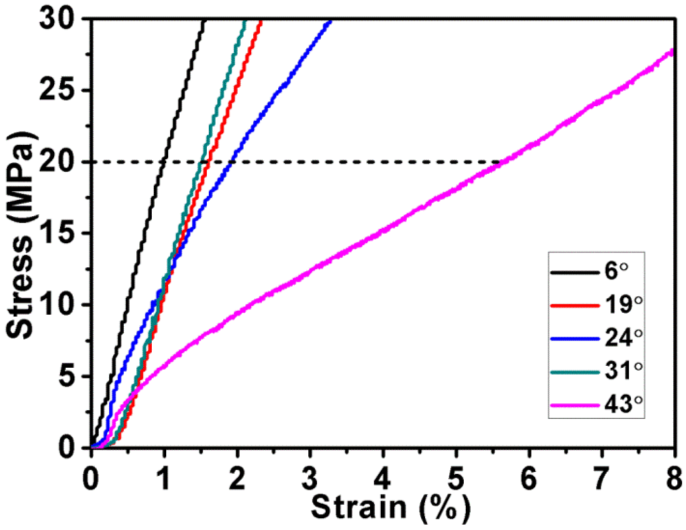

Figure S19. Stress-strain curves of the secondary fibers with increasing secondary helical angles in the starting stage.

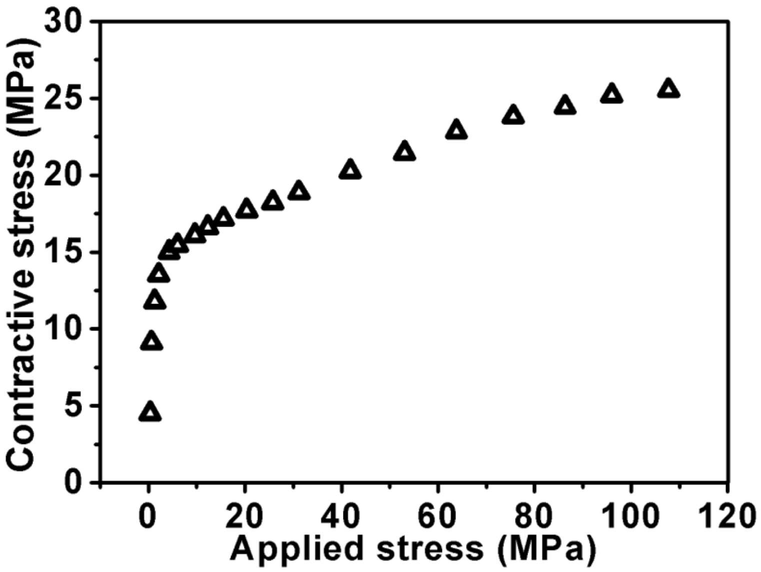

Figure S20. Dependence of the contractive stress on the applied stress for a secondary fiber (helical angle of appropriately 31 °) upon the pass of a current of 125 mA.

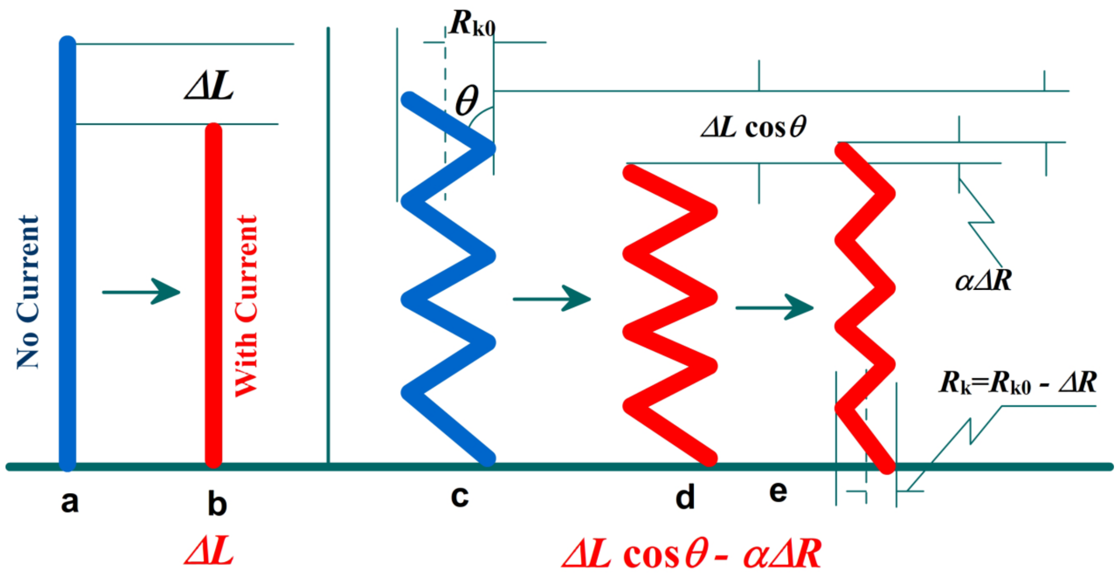

Figure S21. A non-helical MWCNT bundle being assumed to shrink from **a** to **b** with a decreased length of ΔL after pass of the current. **c** corresponds to a helical MWCNT bundle with a helical angle of θ without pass of the electric current. **d** and **e** correponds to the fiber at **c** being shortened by $\Delta L \cos\theta$ and ($\Delta L \cos\theta - \alpha\Delta R$) before and after considering the radial tightening effect produced by the Lorentz force.